ACS Catalysis

Research Article

Cite This: ACS Catal. 2018, 8, 9625−9636

pubs.acs.org/acscatalysis

Unraveling the Chemical State of Cobalt in Co-Based Catalysts during Ethanol Steam Reforming: an in Situ Study by Near Ambient Pressure XPS and XANES

Cristián Huck-Iriart,[†,‡] Lluís Soler,[§] Albert Casanovas,[§] Carlo Marini,[†] Jordi Prat,[†] Jordi Llorca,*[,§] and Carlos Escudero*[,†]

[†]ALBA Synchrotron Light Source, Carrer de la Llum 2-26, 08290 Cerdanyola del Vallès, Barcelona, Spain

[‡]Escuela de Ciencia y Tecnología, Universidad Nacional de San Martín (UNSAM), Campus Miguelete, 25 de Mayo y Francia, 1650 San Martín, Provincia de Buenos Aires, Argentina

[§]Institute of Energy Technologies, Department of Chemical Engineering and Barcelona Research Center in Multiscale Science and Engineering, Universitat Politècnica de Catalunya, EEBE, Eduard Maristany 10-14, 08019 Barcelona, Spain

Supporting Information

ABSTRACT: The steam reforming of ethanol (ESR) has been studied by near ambient pressure XPS (NAP-XPS), extended X-ray absorption fine structure (EXAFS), and X-ray absorption near edge structure (XANES) under in situ conditions in the ALBA synchrotron facility at 200−580 °C and S/C = 3 over different cobalt-based catalysts that showed different catalytic performances: $Co_3[Si_2O_5]_2(OH)_2$ (Co-talc), $[Co_2Mg_4Al_2(OH)_{16}]CO_3{\cdot}4H_2O$ (Co-hydrotalcite shortened to Co-HT) calcined at 550 °C, and Co_3O_4 (Co-spinel). Both Co-spinel and Co-talc yield to a greater or lesser degree metallic cobalt under ESR conditions. While Co-spinel shows a complete reduction to metallic cobalt under the conditions used for the XANES measurements, the more bulk-sensitive Co-talc sample exhibits only a partial reduction. On the other hand, under the ESR conditions used with the NAP-XPS, a more surface sensitive technique, the results indicate a higher reduction degree for the Co-talc sample in comparison to the Co-spinel sample. In contrast, the catalyst prepared from the Co-HT does not show metallic cobalt traces under the experimental conditions used with both techniques. On comparison of these three cobalt-based catalysts, the stable operation exhibited by Co-HT under ESR reaction conditions is justified by the absence of metallic cobalt formation under in situ conditions, which is identified as being responsible for the carbon deposition phenomenon that triggers the deactivation suffered by most cobalt-based catalysts during ESR.

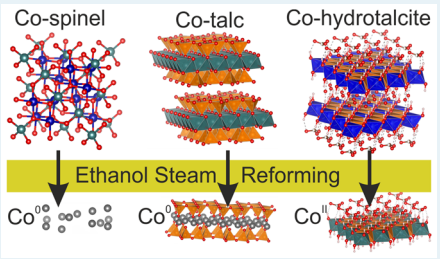

KEYWORDS: *cobalt talc, cobalt hydrotalcite, cobalt spinel, ethanol steam reforming, in situ spectroscopy, NAP-XPS, XANES*

Downloaded by UNIV NACIONAL DE SAN LUIS at 13:11:15:157 on June 24, 2019
from https://pubs.acs.org/doi/10.1021/acscatal.8b02666.

1. INTRODUCTION

The steam reforming of ethanol (ESR) is a well-known process used for generating hydrogen (eq 1). It is particularly interesting for the on-site and on-board production of hydrogen due to the widespread use of ethanol and its safe transport and storage.[1,2] The steam reforming of renewable bioethanol (ethanol produced from biomass by fermentation) can be considered CO_2 neutral because the CO_2 yielded in the reaction is compensated by the CO_2 fixed by the biomass during its growth. Therefore, ESR is emerging as a cleaner alternative to generate hydrogen in comparison to the fossil fuels currently used. Recently, the use of microreaction technologies and catalytic membrane reactors have allowed strong process intensification, which in turn has increased the interest in ESR for feeding fuel cells in transportation and electronic applications.[3−6]

$$C_2H_5OH + 3H_2O \leftrightarrows 6H_2 + 2CO_2 \quad (1)$$

The reaction network associated with the ESR is complex, from both mechanistic and thermodynamic points of view.[7] The intermediate steps involved include a variety of reaction types (dehydration, dehydrogenation, reforming, WGS, methanation, etc.). They show different dependence relationships on reaction conditions, and their promotion depends on different functionalities of the catalyst. In addition, formation of coke precursors from several of the compounds involved makes deactivation an important issue for the practical application of this process, which can be partially solved by the addition of alkaline promoters.[8−10] All of these factors explain the need for extensive research of appropriate catalysts. Many studies have been focused on the ESR using supported nickel, cobalt, and noble-metal catalysts.[11−15] An efficient catalyst for hydrogen production from ethanol has to dissociate the C−C bond at reasonably low temperatures, and it has to maintain a low CO concentration and be stable under catalytic operation.

Received: July 9, 2018
Revised: September 3, 2018
Published: September 6, 2018

© 2018 American Chemical Society

DOI: 10.1021/acscatal.8b02666
ACS Catal. 2018, 8, 9625−9636

Noble-metal-based catalysts perform well for ESR; they are stable and exhibit high activity.[16−18] However, they are expensive and usually need high temperatures to be active. The main reaction mechanism involves the decomposition of ethanol into a mixture of hydrogen, carbon monoxide, and methane (eq 2), followed by the steam reforming of the produced methane (eq 3).[19] Additionally, the water-gas shift (WGS) reaction balances CO and CO_2, rendering extra hydrogen amounts (eq 4). Nickel catalysts are inexpensive and follow the same reaction scheme, but they normally suffer from sintering and deactivation by carbon deposition.[1] In contrast, cobalt-based catalysts can operate at much lower temperature levels in comparison with noble-metal- and nickel-based catalysts, typically at 400−550 °C, since they do not yield methane as an intermediate species in the reaction mechanism, which can only be reformed at high temperature.[20−27] Over cobalt-based catalysts, ethanol is first dehydrogenated into a mixture of hydrogen and acetaldehyde (eq 5), and then acetaldehyde reacts with steam to yield hydrogen and carbon monoxide (eq 6), which participate in the WGS (eq 4). Dimethyl ketone can be also formed via condensation of acetaldehyde. A complete network of reactions can be found in the literature.[7,17]

$$C_2H_5OH \leftrightarrows H_2 + CO + CH_4 \quad (2)$$

$$CH_4 + H_2O \leftrightarrows 3H_2 + CO \quad (3)$$

$$CO + H_2O \leftrightarrows H_2 + CO_2 \quad (4)$$

$$C_2H_5OH \leftrightarrows H_2 + CH_3CHO \quad (5)$$

$$CH_3CHO + H_2O \leftrightarrows 3H_2 + 2CO \quad (6)$$

An important advantage of conducting the ESR at lower temperature is that the WGS equilibrium favors the formation of hydrogen and CO_2 at the expense of CO and water (eq 4), thus maximizing the production of H_2 and reducing the volume of the WGS units normally implemented downstream from the reformer. However, most cobalt catalysts also suffer from severe deactivation during ESR due to extensive carbon deposition,[11−13,28−30] particularly under realistic loads of ethanol. The coke formation on the catalyst surface has been related to the presence of metallic Co sites that would act as nucleation points for its growth, but there still is controversy among different reports. Essential for this matter is an understanding of the role of the cobalt oxidation state.

In a pioneering study by in situ magnetic measurements, it was first demonstrated that metallic cobalt is a very active species for the reforming of ethanol.[31] A Co/ZnO catalyst showed 92% of reduced cobalt under ESR conditions, mainly as small superparamagnetic nanoparticles. However, on the same catalyst, in situ FTIR with CO as a probe molecule revealed that, in addition to metallic cobalt, oxidized Co species were also present at the surface, thus suggesting that the redox pair $Co^0 \leftrightarrows Co^{\delta+}$ is responsible for the activity of cobalt in ESR.[32] Since then, the exact role of Co^0 and $Co^{\delta+}$ during ESR has been investigated over several cobalt-based catalysts with a variety of in situ and operando techniques with great success, and it has been recognized that the oxidation state of Co depends on many different factors such as the catalyst structure, particle size, support material, and composition of the gas phase in the reaction environment, among others.[33−42] In particular, considerable efforts have been addressed toward the Co/CeO_2 system due to the large oxygen storage capacity and high oxygen mobility exhibited by ceria that prevent extensive carbon deposition during ESR. It has been reported that a proper metal−support interaction allows only partial reduction of cobalt and leads to a superior catalytic performance for the production of hydrogen. Specifically, $Co^{\delta+}$ with O adatoms supplied by a reducible support facilitates the oxidative dehydrogenation of ethoxide to acetaldehyde, while the reduced Co^0 subsequently decomposes the acetaldehyde to reforming products.[43] However, inconsistent results regarding the role of the oxidized cobalt species have been presented for non-reducible supports. Over Al_2O_3 a balanced Co^0:$Co^{\delta+}$ ratio of about 3:1 has been reported to be optimum for stable ESR performance,[39] but over MgO it has been suggested that $Co^{\delta+}$ should be minimized to avoid methanation activity.[44] To conclude, results have highlighted the importance of the oxidation state of cobalt in determining the activity, selectivity, and stability of cobalt-based catalysts for ESR, but no conclusion has been made regarding the different inorganic oxide supports and their interactions with cobalt, which calls for more investigations upon the active sites in working cobalt catalysts under ESR conditions. Therefore, a study of the cobalt oxidation state of Co-based catalysts under in situ and operando conditions is crucial to evaluate the catalyst behavior under more realistic ESR conditions and can offer new insights regarding its role in the activation/deactivation phenomena.

The aim of this work is the study of Co-spinel, Co-hydrotalcite (abbreviated as Co-HT from now on), and Co-talc in bulk and at the surface, employing in situ X-ray absorption near edge structure (XANES), in situ extended X-ray absorption fine structure (EXAFS), and near ambient pressure X-ray photoemission spectroscopy (NAP-XPS), in order to understand the behavior of these catalysts under ESR conditions. Co-spinel (Co_3O_4) has been selected as a standard material, whereas Co-talc ($Co_3[Si_2O_5]_2(OH)_2$) and Co-HT ($[Co_2Mg_4Al_2(OH)_{16}]$-$CO_3{\cdot}4H_2O$) have been chosen due to their radically different catalytic performances in ESR. Over Co-talc and Co-spinel, metallic Co nanoparticles are formed easily under ESR conditions at 400 °C, which rapidly detach from the catalyst support and originate carbon nanotubes, nanofibers, and platelets. The carbon deposition rate measured at S/C = 3 is ca. 30 $mg_{carbon}\ g_{catalyst}^{-1}\ h^{-1}$ for both Co-spinel and Co-talc.[45] At the same time, selectivity to methane and higher hydrocarbons increases at the expense of the reforming products (H_2 and CO_x).[46,47] In contrast, the catalyst derived from Co-HT shows an excellent performance for ESR at 550 °C (H_2 yield of 92%) and no metallic cobalt is apparently formed.[48] In this case, the carbon deposition rate measured at S/C = 2 is only about 1 $mg_{carbon}\ g_{catalyst}^{-1}\ h^{-1}$.[48]This interesting result allows the design of cobalt-based catalysts for ESR without coke deposition by placing in appropriate environments $Co^{\delta+}$ active species. Long-term catalytic tests (300 h) under high loads of ethanol and commercial bioethanol have shown stable operation over hydrotalcite-derived cobalt catalysts without carbon deposition.[49,50]

2. MATERIALS AND METHODS

2.1. Catalyst Preparation. Co-spinel, Co_3O_4, was prepared by the citrate method from $Co(NO_3)_2{\cdot}6H_2O$ and citric acid as has been previously described.[51] Co-talc, $Co_3[Si_2O_5]_2(OH)_2$, was obtained by following the procedure described in the literature.[47] Co-HT, $[Co_2Mg_4Al_2(OH)_{16}]CO_3{\cdot}4H_2O$, was prepared by coprecipitation at constant pH (10 ± 0.2) by adding an aqueous solution of NaOH/Na_2CO_3 (2 M) to an

DOI: 10.1021/acscatal.8b02666
ACS Catal. 2018, 8, 9625−9636

aqueous solution of $CoCl_2{\cdot}6H_2O$, $Mg(NO_3)_2{\cdot}6H_2O$, and $Al(NO_3)_3{\cdot}9H_2O$. The slurry was aged at 25 °C for 15 h with vigorous stirring, and the resulting precipitate was thoroughly washed to eliminate any Na residue and calcined at 823 for 3 h.[49] The resulting material constituted a mixture of CoAl spinel and CoO strongly interacting with MgO, as reported in the literature.[48]

2.2. Characterization Techniques. *2.2.1. X-ray Absorption Near Edge Structure (XANES).* XANES measurements at the Co K edge (7709 eV) were performed in quick-EXAFS transmission mode at the CLAESS beamline[52] of the ALBA Synchrotron Light Source. The synchrotron radiation emitted by a multipole wiggler was first collimated vertically by a first mirror and then monochromated with a liquid nitrogen cooled Si (111) double crystal. The monochromated X-ray beam was then focused down to the sample at about 800 μm × 500 μm ($H \times V$) by changing the radius of curvature of a vertically focusing mirror. The higher harmonics contribution to desired energies was minimized by appropriately setting the rejection angles of the two mirrors in the optical hutch. The incoming and outgoing photon fluxes were measured by ionization chambers filled with an appropriate mixture of N_2 and Kr gases. Beamline energy was calibrated on the edge position of a cobalt foil. The ethanol and water mixture for the ESR was prepared in a bubbler using He as a carrier gas in order to have an ethanol/water ratio of 1/6 in the reactor chamber (S/C = 3). Reactants were introduced into the reactor chamber at atmospheric pressure with control of the flow (20 mL/min).

2.2.2. Extended X-ray Absorption Fine Structure (EXAFS). The EXAFS data at the Co K edge were collected at the CLAESS beamline[52] of the ALBA Synchrotron Light Source, using the same optical configuration and setup employed in the XANES experiments. EXAS data reduction has been performed according to a standard procedure using the DEMETER software package.[53] For each spectrum, the raw data have been normalized by calculating and subtracting pre-edge and post-edge backgrounds as low-order polynomial smooth curves. Successively the EXAFS oscilation signal has been extracted. The useful k range available for the EXAFS analysis was between 2.8 and 12.5 Å^{-1}. A sine window has been used to truncate the EXAFS signal, and a k^2 weighted Fourier transform (FT) of it was used for visualization of the real space distribution of Co local structure.

2.2.3. Near Ambient Pressure X-ray Photoemission Spectroscopy (NAP-XPS). The X-ray photoemission spectra were recorded at the NAPP branch from CIRCE, an undulator beamline with a photon energy range of 100−2000 eV at the ALBA Synchrotron Light Source.[54] The acquisition was performed using a PHOIBOS 150 NAP electron energy analyzer (SPECS GmbH) equipped with four differential pumping stages and a set of electrostatic lenses which enable the performance of XPS measurements with the sample at pressures from ultrahigh vacuum (UHV, with a base pressure of $(2-5) \times 10^{-10}$ mbar) up to 20 mbar. The takeoff angle was approximately 50°, and the angle between the analyzer axis and the incoming synchrotron radiation horizontal linear polarization vector was 54.7°, the magic angle. The spectra were acquired with a 20 μm exit slit, and the diameter of the X-ray spot was estimated to be in the order of 100 μm × 65 μm ($H \times V$). Two different photon energies were used, 965 and 1250 eV, to provide variable surface sensitivity: i.e., the inelastic mean free paths (IMFP) were close to 0.5 and 0.9 nm, respectively.[55] The spectra were acquired with 20 eV pass energy with an overall (analyzer and monochromator) energy resolution lower than 300 meV full width at half-maximum (fwhm): 276 meV for $h\nu$ = 965 eV and 291 meV for $h\nu$ = 1250 eV. For the data analysis, the spectra were calibrated with respect to C 1s (at a binding energy of 284.7 eV) and fitted by Gaussian/Lorentzian convolution functions using the CASAXPS software. The background was modeled by a Shirley background function. The ethanol and water mixture for the ESR was prepared in a bubbler as for the XANES experiments, but using Ar as carrier gas, in order to maintain an ethanol/water ratio of 1/6 in the analysis chamber (S/C = 3). Reactants were introduced into the analysis chamber by means of a leak valve. Another leak valve was used to feed H_2. The NAP-XPS experiments were performed at a sample pressure of 0.1 mbar. The samples were mounted on a stainless steel plate and were heated using an infrared laser with λ 808 nm. The sample temperature was monitored with a K-type thermocouple in direct contact with the samples.

3. RESULTS AND DISCUSSION

3.1. In Situ XANES. The K-edge X-ray absorption near edge structure (XANES) of cobalt has been often used to characterize the bulk of Co-based materials due to the possibility of detecting spectral changes in the near edge features related to the local structural and electronic properties of the compounds. These spectral variations appear as resonances characterized by different energy positions and/or intensities in the prepeak and absorption edge.[56] Figure 1 shows the evolution of the Co K-edge XANES spectra of the three different Co-based materials studied, i.e. Co_3O_4, Co-talc, and Co-HT, under ESR reaction conditions. Additionally, the spectra of five different cobalt compounds are presented in the bottom of the plot to be used as references: (a) $LiCoO_2$, (b) Co_3O_4, (c) CoO, (d) $Co(OH)_2$, (e) metallic Co foil. When the sample temperature is increased from room temperature to 550 °C under ESR reaction conditions, Co K-edge XANES reveals significant changes in the cobalt electronic structure which indicate a reduction process for all of the samples studied. The spinel phase Co_3O_4 exhibits a mixture of Co oxidation states where two-thirds of the total Co ions correspond to trivalent cations in octahedral positions while one-third corresponds to divalent cations occupying tetrahedral sites.[51,57] No significant changes are observed in the pre-edge features on heating from 250 °C up to 400 °C, and only partial reduction to CoO is detected at temperatures of around 400 °C, but above 500 °C, the formation of a metallic cobalt phase masks the contribution of the cations (Figure 1). For the Co-talc system there are no clear spectral changes up to 500 °C, and from this temperature to 550 °C, the spectral features reveal that part of the cobalt is reduced to a metallic phase, as shown in Figure 1, where a clear shoulder at ca. 7709 eV assigned to metallic cobalt appears. However, a different behavior is observed for the Co-HT system. In this case, as for the Co_3O_4 reference sample, there is a partial reduction to Co(II) already detected at 300 °C but there is no further reduction to metallic Co at higher temperatures. The final state for the Co-HT is characterized by an increase of the intensity of the white line and the resonance transitions, and multiple scattering contributions seem to correspond to a combination of CoO and $Co(OH)_2$ phases. Nevertheless, some features such as the pre-edge and oscillation intensities are not fully reproduced by a linear combination. Unlike in the other studied samples, the pre-edge peak for the Co-HT retains the same shape even at 550 °C (see Figure 1) and there is no indication of reduction to metallic Co. In fact, the Co-HT sample has been previously calcined and its

DOI: 10.1021/acscatal.8b02666
ACS Catal. 2018, 8, 9625−9636

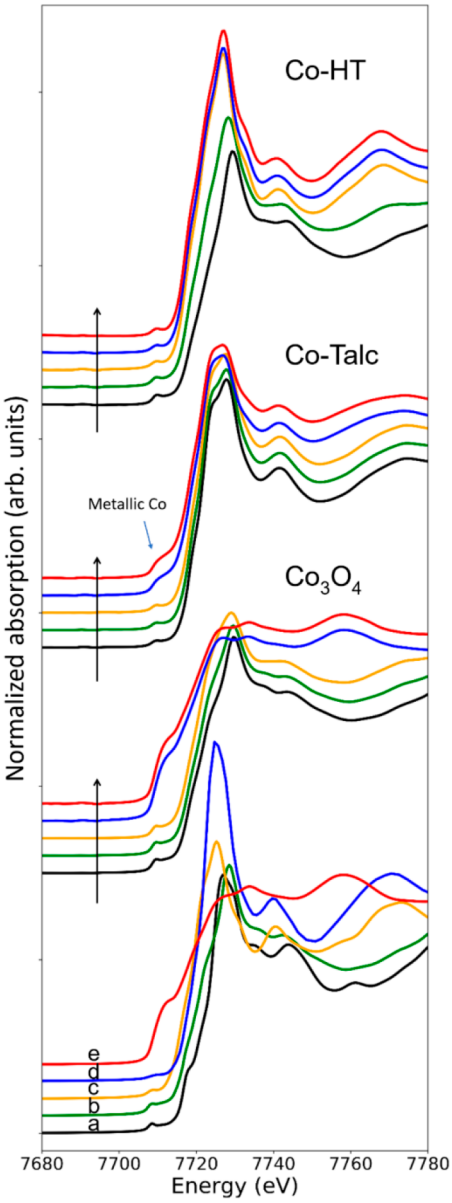

Figure 1. In situ Co K-edge XANES during the ESR reaction at different temperatures for the three tested catalysts: Co_3O_4, Co-talc, and Co-HT. The spectra for each temperature are displayed with different colors: 250 (black), 300 (green), 400 (orange), 500 (blue), and 550 °C (red). At the bottom the spectra for five reference compounds are plotted (all at room temperature): (a) $LiCoO_2$ (black), (b) Co_3O_4 (green), (c) CoO (orange), (d) $Co(OH)_2$ (blue), and (e) Co foil (red).

thermal decomposition yields a well-dispersed mixture of CoAl spinels,[50] which is similar to the case for cobalt spinels, but cobalt is in a more complex environment surrounded by other oxide phases (MgO, Al_2O_3).[48]

The similarities in the spectral features for different chemical environments and the complexity of the reduction pathway in samples such as Co-talc and Co-HT could lead to misinterpretation of the experimental results. However, the cobalt average oxidation state can be easily estimated by considering the energy edge shift in our samples and other standard cobalt compounds and using integral methods as described by Capehart et al.[58] This approach has been already applied in order to follow the reduction process of Co in bulk materials.[59]

Figure 2a shows the calibration curve obtained using metallic Co, CoO, Co_3O_4, and $LiCoO_2$ as reference compounds and

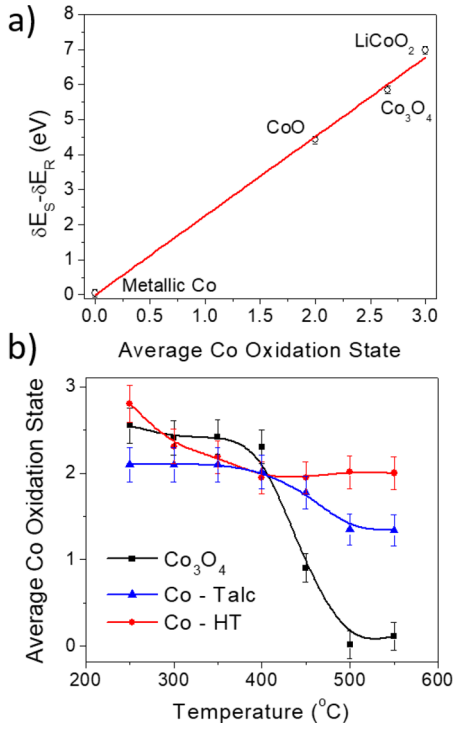

Figure 2. (a) Calibration curve employing different oxide references. These values have been calculated using integral methods as described by Capehart et al.[58] (see the Supporting Information). The curve slope was 2.26 ± 0.08 with R^2 = 0.996. (b) Average oxidation state of the bulk material under ESR reaction conditions as a function of temperature.

employing this integral method (a more detailed description of its application can be found in the Supporting Information). In this way it is possible to get the evolution of the average oxidation state of the samples studied under ESR conditions and different temperatures (Figure 2b). Co_3O_4 shows a slight decrease of the average oxidation state from 250 to 400 °C which correlates with the partial formation of CoO described from the spectral evolution in Figure 1, but from 400 to 500 °C a dramatic reduction to the metallic state is observed. The average charge of Co ions in the Co-talc sample at 250 °C is close to 2.1 ± 0.2, probably due to different local environments and strong interactions within the silicate matrix that would also explain the different spectral features observed with respect to the CoO reference sample. Then, when the temperature is increased to 500 °C, the Co oxidation state decreases to 1.4 ± 0.2, which indicates the partial reduction to metallic Co and therefore the presence of a mixture of chemical phases as shown in the near edge features (Figure 1). On the other hand, Co-HT exhibits an oxidation state of close to 3 at 250 °C which smoothly decreases one unit at 400 °C, and no further reduction is observed at higher temperatures. For this sample there are no insights into metallic Co formation as stated when the XANES spectra are discussed.

More detailed information has been obtained for Co_3O_4, Co-talc, and Co-HT systems through chemical speciation by a linear combination of XANES references. Co_3O_4, CoO, and metallic Co were employed to analyze the Co_3O_4 reduction under ESR conditions (Figure 3a). The references used to analyze the behavior of Co-talc under ESR conditions were Co-talc (the

DOI: 10.1021/acscatal.8b02666
ACS Catal. 2018, 8, 9625−9636

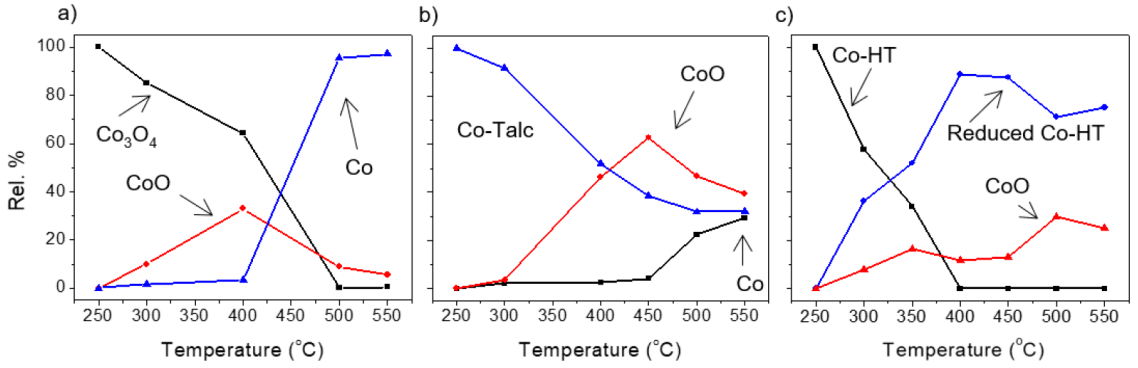

Figure 3. Relative component composition for (a) Co_3O_4, (b) Co-talc, and (c) Co-HT samples under ESR reaction conditions as a function of temperature (R^2 is higher than 0.996 in all cases).

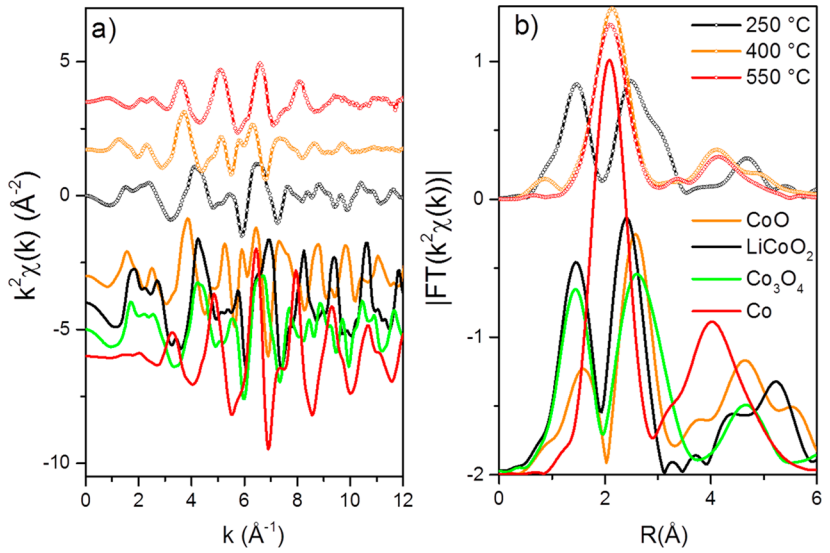

Figure 4. (a) Raw EXAFS data for the Co_3O_4 sample under ESR reaction conditions and at increasing temperatures. (b) Corresponding Fourier transformations. The spectra for each temperature are displayed with different colors: 250 (black), 400 (orange), and 550 °C (red). At the bottom the spectra for four reference compounds are plotted (all at room temperature): $LiCoO_2$ (black), Co_3O_4 (green), CoO (orange), and (e) Co foil (red).

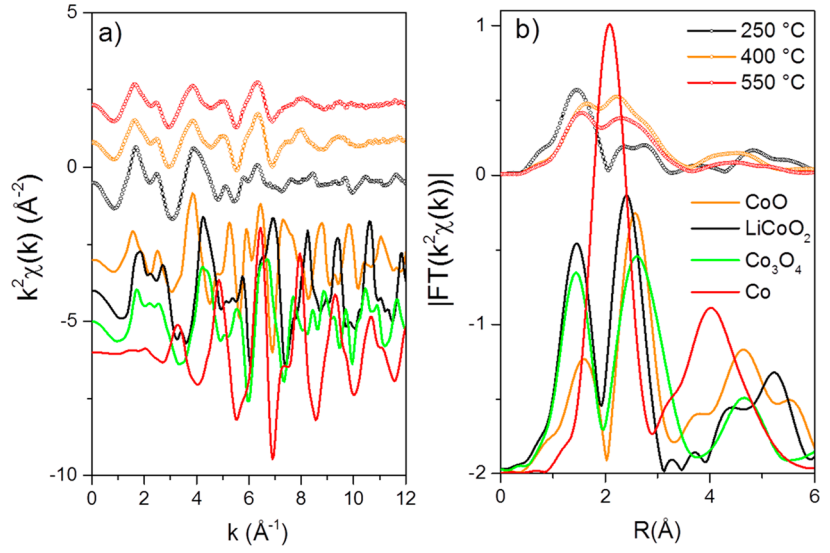

Figure 5. (a) Raw EXAFS data for the Co-talc sample under ESR reaction conditions and at increasing temperatures. (b) Corresponding Fourier transformations. The spectra for each temperature are displayed with different colors: 250 (black), 400 (orange), and 550 °C (red). At the bottom the spectra for four reference compounds are plotted (all at room temperature): $LiCoO_2$ (black), Co_3O_4 (green), CoO (orange), and (e) Co foil (red).

DOI: 10.1021/acscatal.8b02666
ACS Catal. 2018, 8, 9625−9636

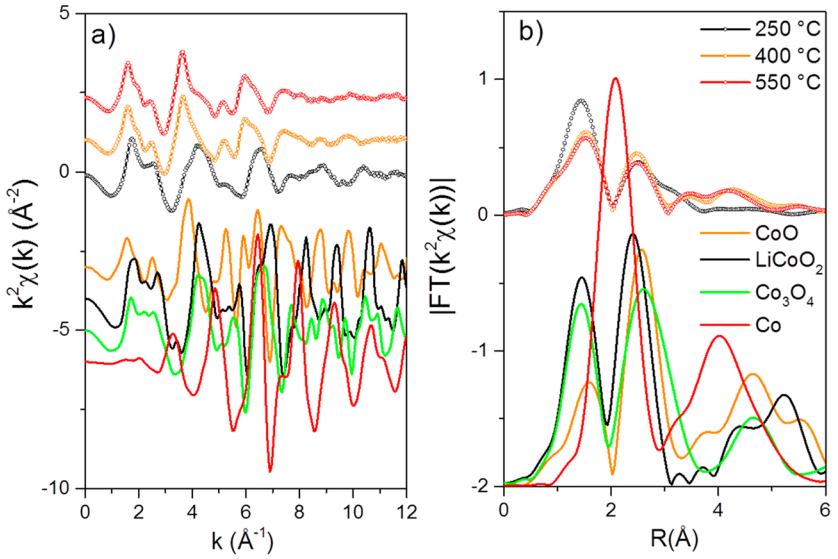

Figure 6. Raw EXAFS data for the Co-HT sample under ESR reaction conditions and at increasing temperatures. (b) Corresponding Fourier transformations. The spectra for each temperature are displayed with different colors: 250 (black), 400 (orange), and 550 °C (red). At the bottom the spectra for four reference compounds are plotted (all at room temperature): $LiCoO_2$ (black), Co_3O_4 (green), CoO (orange), and (e) Co foil (red).

same sample measured at room temperature under He atmosphere), CoO, and metallic Co (Figure 3b), while the selected references to analyze the chemical changes of Co-HT were the original Co-HT, CoO, and Co-HT after H_2 reduction (denoted Reduced Co-HT), as illustrated in Figure 3c. The selection of these references was based on the similarities of their spectral features with those shown by the samples studied at different temperatures. For both samples, Co_3O_4 and Co-talc, the cobalt reduction to the metallic form is through a Co(II) intermediate (most likely CoO). For Co_3O_4 the formation of metallic Co at 500 °C is already close to 100% (Figure 3a). On the other hand, for Co-talc, previous crystallographic measurements reported for similar nanocomposites revealed that phase segregation takes place through delamination of the talc nanolayers under ESR reaction conditions.[47] Figure 3b shows that Co-talc treated at 550 °C still has around 32% of the cobalt inside the matrix, 40% as CoO and 28% as metallic Co. From the results at this temperature, the average oxidation state calculated for Co is 1.47 ± 0.06 (this value depends on the formal charge assigned to the Co in Co-talc, in this case considered as +2.1), which is in agreement with the value obtained by the integral method. Co-HT, initially with an average oxidation state of approximately +2.8 (denoted Co-HT in Figure 3c), yields Reduced Co-HT (as denoted in Figure 3c) with an average oxidation state close to +2 even below 400 °C. In this case, it was not possible to complete the spectral fitting with only these two contributions (Co-HT and Reduced Co-HT), and a third component was required in order to improve the linear fit. The features for the third contribution were very similar to those for the CoO phase, and this contribution was more important at high temperatures than at near 400 °C. Although the complexity in which different phases can coexist in this sample under different conditions has been remarked, this assumption worked well for explaining the reduction behavior in a simple way.

3.2. In situ EXAFS. Figure 4a shows the raw EXAFS data acquired in situ under ESR reaction conditions and at different temperatures for Co_3O_4 and Figure 4b their corresponding Fourier transforms (FTs). Following the results of the linear combination analysis of the XANES, and on comparison to the reference spectra, the Co_3O_4 pure fraction progressively decreases in favor of CoO and metallic Co. Coherently the EXAFS signals can be analyzed as a combination of these three phases. The analysis of the other samples, Co-talc and Co-HT, is complex due to the multiple phases present. Under reaction conditions similar to those for Co_3O_4, the raw EXAFS data and the corresponding FT for Co-talc and Co-HT are shown in Figures 5 and 6, respectively. In a way similar to that for Co_3O_4, Co-talc EXAFS signals change significantly during the reaction and, in agreement with the results of the linear combination analysis of the XANES, the Co-talc fraction also progressively decreases in favor of CoO and metallic Co, but to a lesser extent than for the Co_3O_4 sample. Nevertheless, unlike the case for Co_3O_4 and Co-talc, Co-HT EXAFS signals do not change significantly during the ESR reaction at different temperatures, which again is in agreement with the XANES results exposed above and supports that metallic Co is not formed for this sample.

3.3. In Situ Near Ambient Pressure XPS (NAP-XPS). The surface and subsurface regions constitute the active part of the catalyst in catalytic heterogeneous reactions, since it is the part that interacts with the reactant gases. X-ray photoemission spectroscopy (XPS) is a technique traditionally used under high-vacuum conditions that allows studying the composition and electronic structure of surfaces. Since the results from experiments performed ex situ under vacuum conditions can differ from those obtained under more realistic environments, XPS, among other techniques, has been further improved in order to break or diminish the so-called pressure gap.[60] In the case of XPS, the implementation of a differentially pumping system and a set of electrostatic lenses have enabled to work at near ambient pressures with good statistics.[61−63] The possibility of studying samples under different gas mixtures has proved that the surface composition directly depends on the reaction environment, among other factors, pointing out the need to measure under operando or in situ conditions.[18,64]

In situ NAP-XPS measurements were done in order to study the chemical state and local environment of cobalt during the ESR reaction, thus providing information about its surface

DOI: 10.1021/acscatal.8b02666
ACS Catal. 2018, 8, 9625−9636

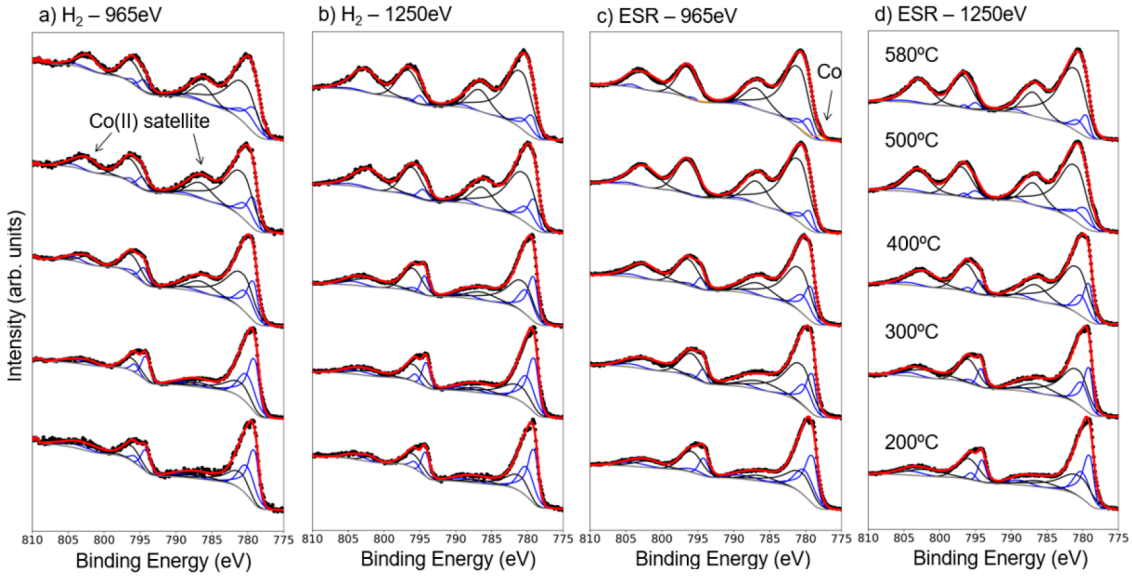

Figure 7. In situ near ambient pressure Co $2p_{3/2}$ XPS for Co_3O_4 exposed to H_2 (a, b) and ESR atmospheres (c, d). The experiments were carried out at different temperatures as indicated in the right panel with two different photon incidence energies: 965 eV (a, c) and 1250 eV (b, d). Legend: Co_3O_4, blue lines; CoO, black lines; metallic Co, orange lines; background, gray lines; the envelope, red lines.

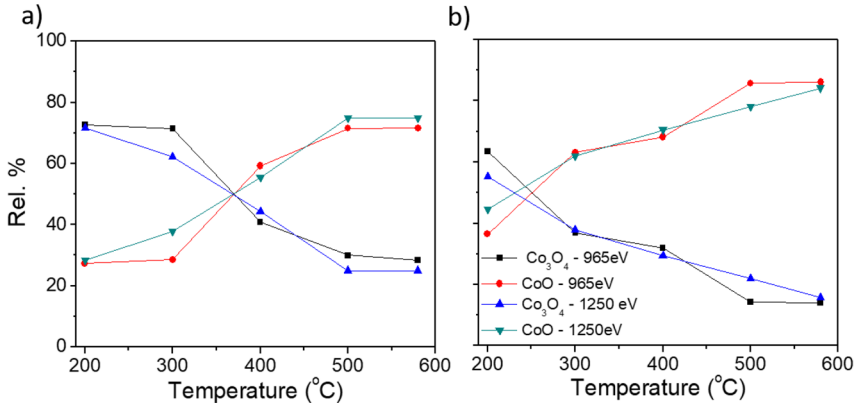

Figure 8. Relative surface composition (Co_3O_4 vs CoO) as a function of temperature and penetration depth for (a) pure H_2 and (b) ESR reaction mixture.

chemistry and complementing the bulk information obtained by XANES. In order to understand the catalyst behavior under the ethanol/water reaction atmosphere used for the ESR reaction, where H_2 is generated and creates a local reducing environment, the catalysts were also exposed in a separate experiment (with a different pellet made from the same sample) to pure H_2 to compare the final state for both experimental conditions. For all of the samples, spectra were acquired under in situ conditions at 0.1 mbar and room temperature, and then the temperature was increased while the pressure was kept constant.

The C 1s signal did not show significant changes under ESR reaction conditions (Figure S5) for all of the samples studied. Taking into account the amount of carbon deposition measured in our previous catalytic tests,[45−48] longer reaction times are required to follow the evolution of the C 1s signal, which was not possible due to beamtime limitation.

The interpretation of Co XP spectra is not straightforward due to peak asymmetries, binding energy (BE) overlap of the metallic and oxide species and their satellites, the different complex environments present in Co-talc and Co-HT samples, and the charging effects. In order to minimize the uncertainty and error in the peak assignment process, the data treatment has been done according to the procedure reported by Biesinger et al.,[65] which describes in detail the curve-fitting procedure for various chemical states of Co-containing samples. Following this reference, only the more intense components and their satellites have been considered in a more simplified way to facilitate the interpretation of the results. In spite of the complications in measuring nonconductive samples such as Co-talc, or samples exhibiting complex environments, such as Co-talc and Co-HT, a clear evolution is observed in all cases, as illustrated below.

3.3.1. Co_3O_4. Figure 7 shows the XP spectra of Co_3O_4 under H_2 (Figure 7a,b) and ESR conditions (Figure 7c,d) with two different incident photon energies to provide information at different depths: 965 eV (Figure 7a,c) and 1250 eV (Figure 7b,d). There is a common trend in both gas environments: a progressive reduction of Co_3O_4 on heating. At 200 °C, the spectra under an ESR mixture and H_2 show the typical shape for the Co_3O_4 cubic normal spinel structure, which exhibits one-third of tetrahedrally coordinated Co^{2+} and two-thirds of octahedrally coordinated Co^{3+}. Nevertheless, at the highest temperature tested (580 °C) the samples are reduced to CoO

DOI: 10.1021/acscatal.8b02666
ACS Catal. 2018, 8, 9625−9636

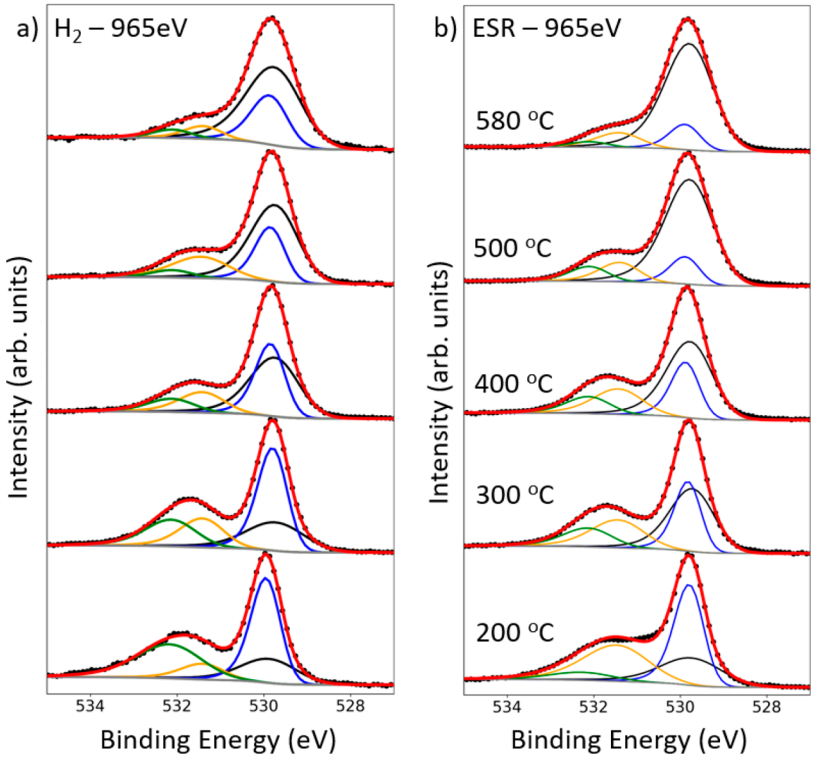

Figure 9. In situ near ambient pressure O 1s XPS (acquired with 965 eV photon energy) of Co_3O_4 exposed to (a) H_2 and (b) ESR atmospheres. The experiments were carried out at different temperatures, as indicated in the right panel. The contribution of water or alcohol bonded to the surface region is displayed in green and the contribution of the hydroxide (or hydrated) oxide in orange. The black line represents the Co_3O_4 contribution and the blue line the CoO contribution. The weight of each compound was estimated by the Co $2p_{3/2}$ fitting procedure described previously.[65]

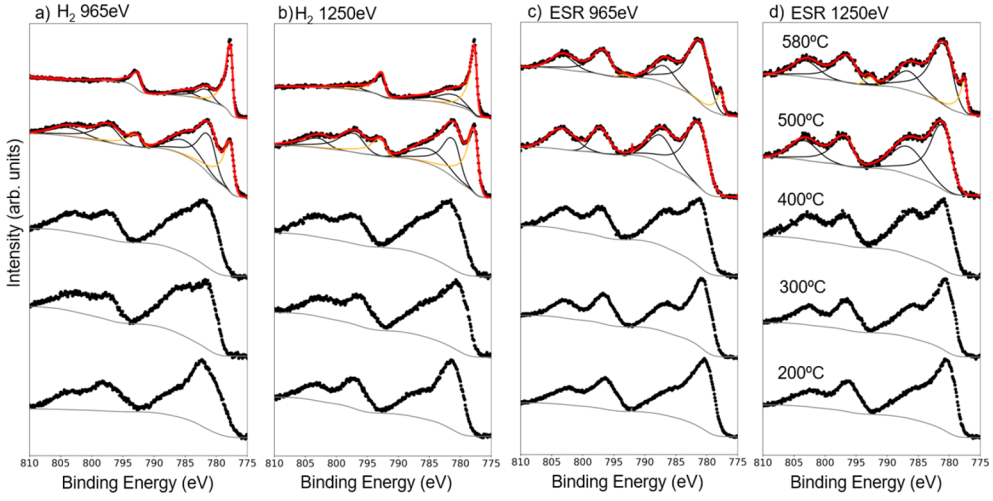

Figure 10. In situ near ambient pressure Co $2p_{3/2}$ XPS for Co-talc exposed to H_2 (a, b) and ESR atmosphere (c, d). The experiments were carried out at different temperatures, as indicated in the right panel, and with two different photon incidence energies: 965 eV (a, c) and 1250 eV (b, d). Legend: Co^{2+}, black lines; metallic Co, orange lines; background, gray lines; the envelope, red lines.

(or hydroxide), and metallic cobalt traces are detected during ESR conditions but not under an H_2 atmosphere. The peak associated with the main Co $2p_{3/2}$ component of Co_3O_4 (779.6 eV) is sharper and is at slightly lower energy than that corresponding to CoO (780.0 eV and similar values for the hydroxide species).[65] In addition, Co_3O_4 exhibits a weak shakeup satellite at higher binding energies (around 10 eV from the main peak), while CoO has a characteristic strong satellite at 786 eV (around 6 eV above the main peak). This strong satellite observed in the CoO photoemission is explained by the octahedrally coordinated, high-spin Co^{2+} oxides, where charge is transferred from the ligand to the 3d orbital, enabling different final states in the photoemission process. Instead, for Co_3O_4 the satellite peak is weaker because two-thirds of the octahedrally coordinated Co^{3+} states do not contribute to charge transfer and only the remaining one-third tetrahedrally coordinated Co^{2+} give rise to shakeup peaks.[66,67]

The evolution of the surface relative composition (Co_3O_4 vs CoO) under a particular gas environment with the temperature (Figure 8) does not show significant differences at different

DOI: 10.1021/acscatal.8b02666
ACS Catal. 2018, 8, 9625−9636

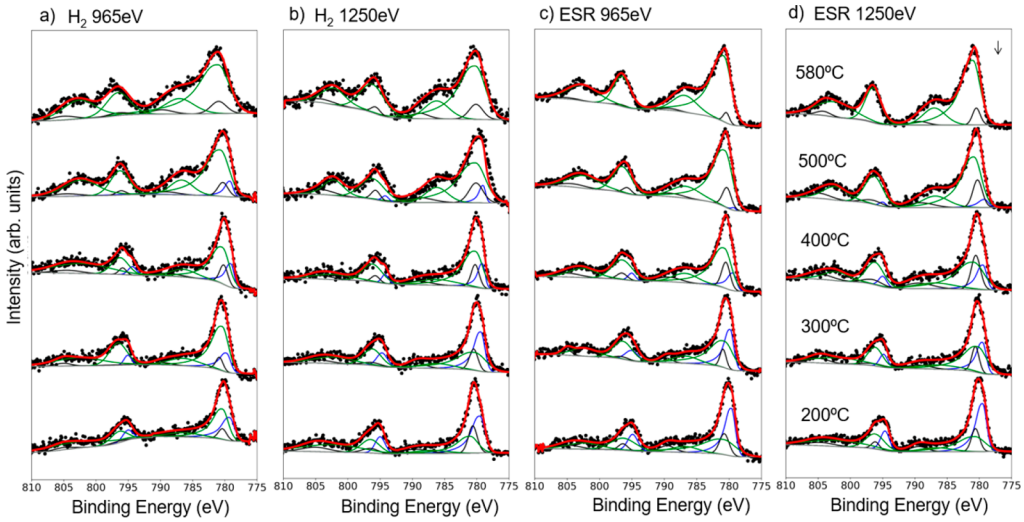

Figure 11. In situ near ambient pressure Co $2p_{3/2}$ XPS of Co-HT exposed to H_2 (a, b) and ESR atmospheres (c, d). The experiments were carried out at different temperatures, as indicated in the right panel, and with two different photon energies: 965 eV (a, c) and 1250 eV (b, d). Legend: Co^{2+} in tetrahedral environments, black lines; high-spin Co^{2+} in octahedral positions, green lines; Co^{3+}, blue lines; background, gray lines; the envelope, red lines.

penetration depths, only a slight surface oxidation under ESR conditions at 200 °C that disappears progressively when the temperature is increased. However, on comparison of the evolution under H_2 with respect to ESR conditions, the sample is more reduced when it is exposed to ESR reaction conditions in the temperature range tested. These results indicate that at the temperatures at which the material is active for hydrogen production the ESR environment is more reducing in comparison to pure H_2. Even at lower temperatures, where the dehydrogenation of ethanol takes place, the sample is overall more reduced under ESR. It is worth noting that traces of metallic Co are detected at 580 °C using 965 eV incidence energy (this was confirmed by increasing the temperature to 660 °C; see Figure S2 in the Supporting Information) while this metallic phase is not observed under H_2 gas.

Figure 9 shows the O 1s spectra of Co_3O_4 obtained with 965 eV photon energy, therefore displaying the most surface sensitive results. The spectra are composed of the contributions from the oxygen lattices of Co_3O_4 and CoO, but the energy separation between the O 1s peaks of both oxides is less than 0.2 eV and it is not possible to resolve them (both with a BE close to ~530 eV). Other contributions to the O 1s signal arise from hydroxide or hydrated oxide species at around ~531.5 eV and from surface-bonded water or organic alcohols at around 532.5 eV.[65] At 200 °C the reduction of cobalt by pure H_2 produces water that hydrates the surface and about 40% of the total O 1s total area corresponds to adsorbed H_2O and hydroxide species, while ESR promotes hydroxide formation, increasing this percentage to 60%. When the temperature is increased to 580 °C, these contributions decay to 13−14% under both H_2 and ESR gas environments and the spectra obtained are equivalent (Figure 9).

3.3.2. Co-talc. In the Co-talc sample, the cobalt ions are embedded in a complex matrix formed by the talc structure, and this fact justifies the broad peaks and satellites obtained for Co 2p spectra (Figure 10). Under both gas environments studied, at lower temperatures (200 °C)—unlike the case for Co_3O_4—there is already a clear satellite which indicates that most of the cobalt corresponds to high-spin Co(II), which is in agreement with the structure of the Co-talc, where the metal occupies octahedral sites with a Co^{2+} oxidation state. However, the peaks are broad due to charging and to the presence of different local environments of the Co atoms within the talc matrix. When Co-talc is heated under H_2 gas, there are changes in the spectra that could be ascribed to Co reorganization or migration up to 400 °C, but it is difficult to assign different components. In this case it can only be noted that there is a clear evolution to metallic Co at higher temperatures (500−580 °C).

Under ESR reaction conditions and high temperatures (400−500 °C) there is a phase segregation process between the talc sheets and CoO (which exhibits a sharper satellite) and then at 580 °C CoO is partially reduced to metallic cobalt, as illustrated in Figure 10c,d. Preliminary transmission electron microscopy studies on similar Co-talc catalysts exposed to ESR reaction conditions (ex situ) revealed the partial formation of metallic Co NPs with a size of 3 nm.[47] This CoO phase transition is not as easily detected under H_2. In this case the reduction to metallic Co at 580 °C is not partial, as observed for ESR conditions, but almost complete. Furthermore, it is worth noting that the metallic Co contribution is greater at higher photon energies (greater penetration length) for both reactive environments. It has been reported that the formation of a very stable 3−5 nm thick CoO phase takes place during redox reactions of Co NPs by a complex mechanism which can inhibit the reaction path to metallic nanoparticles (or reoxidize them into Co_3O_4).[68] The reduction of cobalt under H_2 gas involves cation migration and metallic NP formation, while under ESR reaction conditions, in situ XPS suggests the formation of a CoO phase before reduction which could partially hamper the evolution to metallic Co.

As previously mentioned, in the case of the Co_3O_4 sample metallic Co is only detected as a trace under the ESR reaction conditions studied; therefore, the formation of metallic Co NP from the Co-talc sample exposed to the same experimental conditions could be explained through a combination of surface energy and mechanical tension due to the silicate layer confinement. While for the Co_3O_4 sample the reduction degree is higher under ESR conditions than under a H_2 atmosphere, for the Co-talc sample the measurements under H_2 result in a higher reduction degree in comparison to ESR reaction conditions. In

DOI: 10.1021/acscatal.8b02666
ACS Catal. 2018, 8, 9625−9636

addition, the high water partial pressure in the ESR atmosphere could also hinder the formation of SiO_2, which is formed during the reduction of the Co-talc structure.

3.3.3. Co-HT. Figure 11 shows the analysis of the XP Co 2p spectra for the Co-HT sample acquired with two different photon energies under H_2 gas (Figure 11a,b) and ESR conditions (Figure 11c,d). In all cases there is a clear reduction from Co(III) to Co(II) indicated by a remarkable increase of the satellite attributed to high-spin Co(II) between 500 and 580 °C, but there is no evidence of metallic Co under all the experimental conditions tested. Three contributions were used in order to fit the experimental data: a Co(III) contribution at low energies (∼779 eV), a low-spin Co(II) from a spinel structure at ∼780 eV with a small satellite shifted 9.5−10 eV from the main peak, and finally, a high-spin Co(II) such as CoO oxide with a $2p_{3/2}$ transition at ∼781 eV with a satellite with 6 eV difference from the main peak.

Above 500 °C there are no significant differences between the spectra obtained under both reaction conditions except for the widths of the Co 2p peaks, which are greater when they are measured under pure H_2. The thermal treatment in H_2 reducing media could lead to $CoAl_2O_4$ formation, which exhibits around a 1 eV shift of the Co 2p peak to higher energies with respect to the CoO contribution.[69] Instead, under an ESR atmosphere the Co 2p peaks are narrower and this fact could be attributed to a thin CoO or $Co(OH)_2$ surface layer, which should be more active for hydrogen production in comparison to $CoAl_2O_4$.[34] The presence of MgO could lead to complex dehydrogenation and dehydration routes depending on the temperature conditions,[70] and the generated byproducts along with the presence of water could produce a partial segregation of the cobalt oxide from the main matrix. XP spectra of the Al 2p and Mg 2s regions did not change significantly during the experiments, and they are assigned to their respective oxides (data not shown).

4. CONCLUSIONS

In this work, two different Co-based catalysts, Co-talc and Co-HT, have been studied by in situ XANES, EXAFS, and NAP-XPS under ESR conditions. Moreover, Co_3O_4 spinel has been studied as a reference with the same techniques. Both XANES and NAP-XPS are complementary, since they probe the bulk or surface of the materials studied, respectively. On the one hand, XANES results from bulk analysis show that, while for the standard Co_3O_4 sample there is a complete reduction to metallic Co under ESR at more than 500 °C, under the same conditions Co-talc is only partially reduced to metallic Co and Co-HT does not exhibit metallic Co at all. Co-HT shows a complex environment with the coexistence of different phases, and during the ESR reaction at increasing temperatures the Co is only partially reduced from +2.8 to +2. On the other hand, NAP-XPS measurements have been carried out to study the most superficial layers of these Co-based catalysts interacting with ESR and H_2 gas environments at different temperatures. For Co_3O_4 there is a partial reduction of the initial spinel phase to CoO under both gases by increasing the temperature. In this case, at the highest temperature and at the lowest excitation energy, i.e. the most surface sensitivity, metallic Co traces are detected during ESR but not under H_2. This would imply a more reducing environment under ESR (which generates H_2 locally) in comparison to H_2. Compiling the results from both techniques and considering the unavoidable pressure gap (XANES experiments are performed at atmospheric pressure while NAP-XPS experiments are restricted to the mbar pressure range), we could infer that metallic Co will be formed under realistic ESR pressure conditions. Furthermore, it must be considered that the reduction of CoO produces water, which must segregate from the inner layers toward the material surface. For the case of Co-talc, the obtained NAP-XPS results show a partial reduction to metallic Co, as observed with XANES, which could be attributed to the segregation of metallic Co NPs. This also agrees with previous publications reporting the formation of Co metallic nanoparticles under ESR reaction conditions. In this case, the formation of metallic Co is higher in the case of H_2 gas in comparison to ESR and this could be explained by the formation of a CoO layer in the latter case which may partially obstruct the obtention of Co^0. Finally, the Co-HT sample does not show any indication of metallic Co by NAP-XPS under any of the environments tested, corroborating the XANES results. The evolution with temperature of the XP spectra under H_2 and ESR show a partial reduction from Co(III) to Co(II), as indicated by the increase in the satellite attributed to high-spin Co(II). Our experimental findings support the hypothesis that correlates the deactivation of Co catalysts under ESR reaction conditions with the nucleation and growth of carbon on metallic Co sites. For Co-spinel and Co-talc it has been previously described how carbon nanostructures cover the catalyst surface decreasing their performance, but Co-HT has demonstrated an excellent behavior and long-term stability under ESR conditions. The results shown in this work confirm that there is no metallic Co formation for Co-HT under in situ ESR, emphasizing the importance of designing Co catalysts with $Co^{\delta+}$ active species under appropriate environments that hinder the formation of metallic Co in order to avoid deactivation by carbon deposition.

■ ASSOCIATED CONTENT

Supporting Information

The Supporting Information is available free of charge on the ACS Publications website at DOI: 10.1021/acscatal.8b02666.

Estimation of cobalt average oxidation state from XANES measurements by applying the method reported by Capehart et al. and supplementary in situ near ambient pressure X-ray photoemission measurements of Co-spinel, Co-talc, and Co-HT (PDF)

■ AUTHOR INFORMATION

Corresponding Authors

*E-mail for J.L.: jordi.llorca@upc.edu.
*E-mail for C.E.: cescudero@cells.es.

ORCID

Cristián Huck-Iriart: 0000-0001-5734-2499
Lluís Soler: 0000-0003-1591-3366
Jordi Llorca: 0000-0002-7447-9582
Carlos Escudero: 0000-0001-8716-9391

Notes

The authors declare no competing financial interest.

■ ACKNOWLEDGMENTS

C.H.-I. acknowledges the Argentinian National Research Council (CONICET) for financial support (he is also a member of the research staff of CONICET). J.L. is a Serra Húnter Fellow and is grateful to the ICREA Academia program and grants MINECO/FEDER ENE2015-63969-R and GC 2017 SGR 128. The authors are grateful for the support of ALBA staff for the

DOI: 10.1021/acscatal.8b02666
ACS Catal. 2018, 8, 9625−9636

successful performance of the measurements at the CIRCE and CLAESS beamlines of the ALBA Synchrotron Light Source.

REFERENCES

(1) Li, D.; Li, X.; Gong, J. Catalytic Reforming of Oxygenates: State of the Art and Future Prospects. *Chem. Rev.* **2016**, *116*, 11529−11653.
(2) Llorca, J.; Cortés, V.; Divins, N. J.; Olivera, R. Hydrogen from Bioethanol. In *Renewable Hydrogen Technologies*; Gandía, L. M., Arzamendi, G., Diéguez, P. M., Eds.; Elsevier: 2013; pP 135−169.
(3) Llorca, J.; Casanovas, A.; Trifonov, T.; Rodríguez, A.; Alcubilla, R. First use of macroporous silicon loaded with catalyst film for a chemical reaction: A microreformer for producing hydrogen from ethanol steam reforming. *J. Catal.* **2008**, *255*, 228−233.
(4) Divins, N. J.; López, E.; Rodríguez, Á.; Vega, D.; Llorca, J. Bio-ethanol steam reforming and autothermal reforming in 3-μm channels coated with RhPd/CeO_2 for hydrogen generation. *Chem. Eng. Process.* **2013**, *64*, 31−37.
(5) Pla, D.; Salleras, M.; Morata, A.; Garbayo, I.; Gerbolés, M.; Sabaté, N.; Divins, N. J.; Casanovas, A.; Llorca, J.; Tarancón, A. Standalone ethanol micro-reformer integrated on silicon technology for onboard production of hydrogen-rich gas. *Lab Chip* **2016**, *16*, 2900−2910.
(6) Koch, R.; López, E.; Divins, N. J.; Allué, M.; Jossen, A.; Riera, J.; Llorca, J. Ethanol catalytic membrane reformer for direct PEM FC feeding. *Int. J. Hydrogen Energy* **2013**, *38*, 5605−5615.
(7) Song, H.; Zhang, L.; Ozkan, U. S. Investigation of the Reaction Network in Ethanol Steam Reforming over Supported Cobalt Catalysts. *Ind. Eng. Chem. Res.* **2010**, *49*, 8984−8989.
(8) Llorca, J.; Homs, N.; Sales, J.; Fierro, J. L. G.; De La Piscina, P. R. Effect of sodium addition on the performance of Co-ZnO-based catalysts for hydrogen production from bioethanol. *J. Catal.* **2004**, *222*, 470−480.
(9) Kim, K. S.; Seo, H. R.; Lee, S. Y.; Ahn, J. G.; Shin, W. C.; Lee, Y. K. TPR and EXAFS studies on Na-promoted Co/ZnO catalysts for ethanol steam reforming. *Top. Catal.* **2010**, *53*, 615−620.
(10) Sharma, Y. C.; Kumar, A.; Prasad, R.; Upadhyay, S. N. Ethanol steam reforming for hydrogen production: Latest and effective catalyst modification strategies to minimize carbonaceous deactivation. *Renewable Sustainable Energy Rev.* **2017**, *74*, 89−103.
(11) Vaidya, P. D.; Rodrigues, A. E. Insight into steam reforming of ethanol to produce hydrogen for fuel cells. *Chem. Eng. J.* **2006**, *117*, 39−49.
(12) Haryanto, A.; Fernando, S.; Murali, N.; Adhikari, S. Current Status of Hydrogen Production Techniques by Steam Reforming of Ethanol: A Review. *Energy Fuels* **2005**, *19*, 2098−2106.
(13) Ni, M.; Leung, D. Y. C.; Leung, M. K. H. A review on reforming bio-ethanol for hydrogen production. *Int. J. Hydrogen Energy* **2007**, *32*, 3238−3247.
(14) Contreras, J. L.; Salmones, J.; Colín-Luna, J. A.; Nuño, L.; Quintana, B.; Córdova, I.; Zeifert, B.; Tapia, C.; Fuentes, G. A. Catalysts for H_2 production using the ethanol steam reforming (a review). *Int. J. Hydrogen Energy* **2014**, *39*, 18835−18853.
(15) Hou, T.; Zhang, S.; Chen, Y.; Wang, D.; Cai, W. Hydrogen production from ethanol reforming: Catalysts and reaction mechanism. *Renewable Sustainable Energy Rev.* **2015**, *44*, 132−148.
(16) Deluga, G. A.; Salge, J. R.; Schmidt, L. D.; Verykios, X. E. Renewable Hydrogen from Ethanol by Authothermal Reforming. *Science* **2004**, *303*, 993−997.
(17) Zanchet, D.; Santos, J. B. O.; Damyanova, S.; Gallo, J. M. R.; Bueno, J. M. C. Toward understanding metal-catalyzed ethanol reforming. *ACS Catal.* **2015**, *5*, 3841−3863.
(18) Divins, N. J.; Angurell, I.; Escudero, C.; Pérez-Dieste, V.; Llorca, J. Influence of the support on surface rearrangements of bimetallic nanoparticles in real catalysts. *Science* **2014**, *346*, 620−623.
(19) Idriss, H.; Scott, M.; Llorca, J.; Chan, S. C.; Chiu, W.; Sheng, P.-Y.; Yee, A.; Blackford, M. A.; Pas, S. J.; Hill, A. J.; Alamgir, F. M.; Rettew, R.; Petersburg, C.; Senanayake, S. D.; Barteau, M. A. A phenomenological study of the metal-oxide interface: the role of catalysis in hydrogen production from renewable resources. *ChemSusChem* **2008**, *1*, 905−910.
(20) Llorca, J.; Homs, N.; Sales, J.; Ramírez de la Piscina, P. Efficient Production of Hydrogen over Supported Cobalt Catalysts from Ethanol Steam Reforming. *J. Catal.* **2002**, *209*, 306−317.
(21) Mariño, F.; Baronetti, G.; Jobbagy, M.; Laborde, M. Cu-Ni-K/γ-Al_2O_3 supported catalysts for ethanol steam reforming: Formation of hydrotalcite-type compounds as a result of metal-support interaction. *Appl. Catal., A* **2003**, *238*, 41−54.
(22) Llorca, J.; Ramírez De La Piscina, P.; Dalmon, J. A.; Sales, J.; Homs, N. Co-free hydrogen from steam-reforming of bioethanol over ZnO-supported cobalt catalysts: Effect of the metallic precursor. *Appl. Catal., B* **2003**, *43*, 355−369.
(23) Batista, M. S.; Santos, R. K.; Assaf, E. M.; Assaf, J. M.; Ticianelli, E. A. High efficiency steam reforming of ethanol by cobalt-based catalysts. *J. Power Sources* **2004**, *134*, 27−32.
(24) Vargas, J. C.; Libs, S.; Roger, A.-C.; Kiennemann, A. Study of Ce-Zr-Co fluorite-type oxide as catalysts for hydrogen production by steam reforming of bioethanol. *Catal. Today* **2005**, *107*−*108*, 417−425.
(25) Frusteri, F.; Freni, S. Bio-ethanol, a suitable fuel to produce hydrogen for a molten carbonate fuel cell. *J. Power Sources* **2007**, *173*, 200−209.
(26) Song, H.; Ozkan, U. S. Ethanol steam reforming over Co-based catalysts: Role of oxygen mobility. *J. Catal.* **2009**, *261*, 66−74.
(27) Sohn, H.; Ozkan, U. S. Cobalt-Based Catalysts for Ethanol Steam Reforming: An Overview. *Energy Fuels* **2016**, *30*, 5309−5322.
(28) Vicente, J.; Montero, C.; Ereña, J.; Azkoiti, M. J.; Bilbao, J.; Gayubo, A. G. Coke deactivation of Ni and Co catalysts in ethanol steam reforming at mild temperatures in a fluidized bed reactor. *Int. J. Hydrogen Energy* **2014**, *39*, 12586−12596.
(29) Chiou, J. Y. Z.; Lai, C. L.; Yu, S. W.; Huang, H. H.; Chuang, C. L.; Wang, C.-B. Effect of Co, Fe and Rh addition on coke deposition over Ni/Ce0.5Zr0.5O2catalysts for steam reforming of ethanol. *Int. J. Hydrogen Energy* **2014**, *39*, 20689−20699.
(30) Iulianelli, A.; Palma, V.; Bagnato, G.; Ruocco, C.; Huang, Y.; Veziroğlu, N. T.; Basile, A. From bioethanol exploitation to high grade hydrogen generation: Steam reforming promoted by a Co-Pt catalyst in a Pd-based membrane reactor. *Renewable Energy* **2018**, *119*, 834−843.
(31) Llorca, J.; Dalmon, J. A.; Ramírez De la Piscina, P.; Homs, N. In situ magnetic characterisation of supported cobalt catalysts under steam-reforming of ethanol. *Appl. Catal., A* **2003**, *243*, 261−269.
(32) Llorca, J.; Homs, N.; Ramírez de la Piscina, P. In situ DRIFT-mass spectrometry study of the ethanol steam-reforming reaction over carbonyl-derived Co/ZnO catalysts. *J. Catal.* **2004**, *227*, 556−560.
(33) Turczyniak, S.; Luo, W.; Papaefthimiou, V.; Ramgir, N. S.; Haevecker, M.; MacHocki, A.; Zafeiratos, S. A Comparative Ambient Pressure X-ray Photoelectron and Absorption Spectroscopy Study of Various Cobalt-Based Catalysts in Reactive Atmospheres. *Top. Catal.* **2016**, *59*, 532−542.
(34) de Lima, A. E. P.; de Oliveira, D. C. In situ XANES study of Cobalt in Co-Ce-Al catalyst applied to Steam Reforming of Ethanol reaction. *Catal. Today* **2017**, *283*, 104−109.
(35) Sohn, H.; Soykal, I. I.; Zhang, S.; Shan, J.; Tao, F.; Miller, J. T.; Ozkan, U. S. Effect of cobalt on reduction characteristics of ceria under ethanol steam reforming conditions: AP-XPS and XANES studies. *J. Phys. Chem. C* **2016**, *120*, 14631−14642.
(36) Turczyniak, S.; Greluk, M.; Słowik, G.; Gac, W.; Zafeiratos, S.; Machocki, A. Surface State and Catalytic Performance of Ceria-Supported Cobalt Catalysts in the Steam Reforming of Ethanol. *ChemCatChem* **2017**, *9*, 782−797.
(37) Bayram, B.; Soykal, I. I.; Von Deak, D.; Miller, J. T.; Ozkan, U. S. Ethanol steam reforming over Co-based catalysts: Investigation of cobalt coordination environment under reaction conditions. *J. Catal.* **2011**, *284*, 77−89.
(38) Turczyniak, S.; Teschner, D.; Machocki, A.; Zafeiratos, S. Effect of the surface state on the catalytic performance of a Co/CeO_2 ethanol steam-reforming catalyst. *J. Catal.* **2016**, *340*, 321−330.
(39) Passos, A. R.; Martins, L.; Pulcinelli, S. H.; Santilli, C. V.; Briois, V. Effect of the balance between Co(II) and Co(0) oxidation states on the catalytic activity of cobalt catalysts for Ethanol Steam Reforming. *Catal. Today* **2014**, *229*, 88−94.

DOI: 10.1021/acscatal.8b02666
ACS Catal. 2018, 8, 9625−9636

(40) Óvári, L.; Krick Calderon, S.; Lykhach, Y.; Libuda, J.; Erdohelyi, A.; Papp, C.; Kiss, J.; Steinrück, H. P. Near ambient pressure XPS investigation of the interaction of ethanol with Co/CeO_2(111). *J. Catal.* **2013**, *307*, 132−139.
(41) Ávila-Neto, C. N.; Liberatori, J. W. C.; Da Silva, A. M.; Zanchet, D.; Hori, C. E.; Noronha, F. B.; Bueno, J. M. C. Understanding the stability of Co-supported catalysts during ethanol reforming as addressed by in situ temperature and spatial resolved XAFS analysis. *J. Catal.* **2012**, *287*, 124−137.
(42) Kim, K. S.; Lee, Y. K. The active phase of NaCo/ZnO catalyst for ethanol steam reforming: EXAFS and in situ XANES studies. *Int. J. Hydrogen Energy* **2010**, *35*, 5378−5382.
(43) Martono, E.; Hyman, M. P.; Vohs, J. M. Reaction pathways for ethanol on model Co/ZnO(0001) catalysts. *Phys. Chem. Chem. Phys.* **2011**, *13*, 9880−9886.
(44) Karim, A. M.; Su, Y.; Engelhard, M. H.; King, D. L.; Wang, Y. Catalytic Roles of Co^0 and Co^{2+} during Steam Reforming of Ethanol on Co/MgO Catalysts. *ACS Catal.* **2011**, *1*, 279−286.
(45) Domínguez, M.; Cristiano, G.; López, E.; Llorca, J. Ethanol steam reforming over cobalt talc in a plate microreactor. *Chem. Eng. J.* **2011**, *176-177*, 280−285.
(46) Domínguez, M.; Taboada, E.; Molins, E.; Llorca, J. Co−SiO_2 aerogel-coated catalytic walls for the generation of hydrogen. *Catal. Today* **2008**, *138*, 193−197.
(47) Domínguez, M.; Taboada, E.; Idriss, H.; Molins, E.; Llorca, J. Fast and efficient hydrogen generation catalyzed by cobalt talc nanolayers dispersed in silica aerogel. *J. Mater. Chem.* **2010**, *20*, 4875.
(48) Espinal, R.; Taboada, E.; Molins, E.; Chimentao, R. J.; Medina, F.; Llorca, J. Cobalt hydrotalcite for the steam reforming of ethanol with scarce carbon production. *RSC Adv.* **2012**, *2*, 2946−2956.
(49) Espinal, R.; Taboada, E.; Molins, E.; Chimentao, R. J.; Medina, F.; Llorca, J. Cobalt hydrotalcites as catalysts for bioethanol steam reforming. The promoting effect of potassium on catalyst activity and long-term stability. *Appl. Catal., B* **2012**, *127*, 59−67.
(50) Espinal, R.; Anzola, A.; Adrover, E.; Roig, M.; Chimentao, R.; Medina, F.; López, E.; Borio, D.; Llorca, J. Durable ethanol steam reforming in a catalytic membrane reactor at moderate temperature over cobalt hydrotalcite. *Int. J. Hydrogen Energy* **2014**, *39*, 10902−10910.
(51) Llorca, J.; Ramírez De La Piscina, P.; Dalmon, J.-A.; Homs, N. Transformation of Co_3O_4 during ethanol steam-re-forming. Activation process for hydrogen production. *Chem. Mater.* **2004**, *16*, 3573−3578.
(52) Simonelli, L.; Marini, C.; Olszewski, W.; Ávila Pérez, M.; Ramanan, N.; Guilera, G.; Cuartero, V.; Klementiev, K. CLÆSS: The hard X-ray absorption beamline of the ALBA CELLS synchrotron. *Cogent Phys.* **2016**, *3*, 1231987.
(53) Ravel, B.; Newville, M. ATHENA, ARTEMIS, HEPHAESTUS: Data analysis for X-ray absorption spectroscopy using IFEFFIT. *J. Synchrotron Radiat.* **2005**, *12*, 537−541.
(54) Pérez-Dieste, V.; Aballe, L.; Ferrer, S.; Nicolàs, J.; Escudero, C.; Milán, A.; Pellegrin, E. Near Ambient Pressure XPS at ALBA. *J. Phys.: Conf. Ser.* **2013**, *425*, 072023.
(55) Powell, C. J.; Jablonski, A. *NIST Electron Inelastic-Mean-Free-Path Database, version 1.2, SRD71*; National Insitute of Standards and Technology: 2010.
(56) Jiang, T.; Ellis, D. E. X-ray absortion near edge structures in cobalt oxides. *J. Mater. Res.* **1996**, *11*, 2242−2256.
(57) de la Peña O'Shea, V. A.; Homs, N.; Pereira, E. B.; Nafria, R.; Ramírez de la Piscina, P. X-ray diffraction study of Co_3O_4 activation under ethanol steam-reforming. *Catal. Today* **2007**, *126*, 148−152.
(58) Capehart, T. W.; Herbst, J. F.; Mishra, R. K.; Pinkerton, F. E. X-ray-absortion edge shifts in rare-earth-transition-metal compounds. *Phys. Rev. B: Condens. Matter Mater. Phys.* **1995**, *52*, 7907−7914.
(59) Krylova, G.; Giovanetti, L. J.; Requejo, F. G.; Dimitrijevic, N. M.; Prakapenka, A.; Shevchenko, E. V. Study of nucleation and growth mechanism of the metallic nanodumbbells. *J. Am. Chem. Soc.* **2012**, *134*, 4384−4392.
(60) Escudero, C.; Salmeron, M. From solid-vacuum to solid-gas and solid-liquid interfaces: In situ studies of structure and dynamics under relevant conditions. *Surf. Sci.* **2013**, *607*, 2−9.
(61) Ogletree, D. F.; Bluhm, H.; Lebedev, G.; Fadley, C. S.; Hussain, Z.; Salmeron, M. A differentially pumped electrostatic lens system for photoemission studies in the millibar range. *Rev. Sci. Instrum.* **2002**, *73*, 3872.
(62) Frank Ogletree, D.; Bluhm, H.; Hebenstreit, E. D.; Salmeron, M. Photoelectron spectroscopy under ambient pressure and temperature conditions. *Nucl. Instrum. Methods Phys. Res., Sect. A* **2009**, *601*, 151−160.
(63) Salmeron, M.; Schlögl, R. Ambient pressure photoelectron spectroscopy: A new tool for surface science and nanotechnology. *Surf. Sci. Rep.* **2008**, *63*, 169−199.
(64) Tao, F.; Grass, M. E.; Zhang, Y.; Butcher, D. R.; Renzas, J. R.; Liu, Z.; Chung, J. Y.; Mun, B. S.; Salmeron, M.; Somorjai, G. A. Reaction-Driven Restructuring of Rh-Pd and Pt-Pd Core-Shell Nanoparticles. *Science* **2008**, *322*, 932−934.
(65) Biesinger, M. C.; Payne, B. P.; Grosvenor, A. P.; Lau, L. W. M.; Gerson, A. R.; Smart, R. S. C. Resolving surface chemical states in XPS analysis of first row transition metals, oxides and hydroxides: Cr, Mn, Fe, Co and Ni. *Appl. Surf. Sci.* **2011**, *257*, 2717−2730.
(66) Petitto, S. C.; Marsh, E. M.; Carson, G. A.; Langell, M. A. Cobalt oxide surface chemistry: The interaction of CoO(100), Co_3O_4(110) and Co_3O_4(111) with oxygen and water. *J. Mol. Catal. A: Chem.* **2008**, *281*, 49−58.
(67) Vaz, C. A. F.; Prabhakaran, D.; Altman, E. I.; Henrich, V. E. Experimental study of the interfacial cobalt oxide in Co_3O_4/α-Al_2O_3 (0001) epitaxial films. *Phys. Rev. B - Condens. Matter Mater. Phys.* **2009**, *80*, 1−7.
(68) Papaefthimiou, V.; Dintzer, T.; Dupuis, V.; Tamion, A.; Tournus, F.; Hillion, A.; Teschner, D.; Hävecker, M.; Knop-Gericke, A.; Schlögl, R.; Zafeiratos, S. Nontrivial redox behavior of nanosized cobalt: New insights from ambient pressure X-ray photoelectron and absorption spectroscopies. *ACS Nano* **2011**, *5*, 2182−2190.
(69) Bhattacharya, A. K.; Hartridge, A.; Mallick, K. K.; Werrett, C. R. Low-temperature decomposition of hydrated transition metal chlorides on hydrous gel substrates. *J. Mater. Sci.* **1996**, *31*, 4479−4482.
(70) Chieregato, A.; Ochoa, J. V.; Bandinelli, C.; Fornasari, G.; Cavani, F.; Mella, M. On the chemistry of ethanol on basic oxides: Revising mechanisms and intermediates in the lebedev and guerbet reactions. *ChemSusChem* **2015**, *8*, 377−388.

DOI: 10.1021/acscatal.8b02666
ACS Catal. 2018, 8, 9625−9636